Supporting Information

Graphene/C-PDA/Carbon Fiber Ternary Heterostructure Network Enables Lightweight Polyimide Composites with Enhanced Electromagnetic Shielding and Thermal Management Capabilities

Xiong Li [1, 4], Wenjing Cao [1, 4], Xiaohui Yang [1, 4], Menghuan Wang [2], Yiyuan Chen [2], Tongle Xu [1, 4], Yu Zhang [1, 4], Na Song [1, 4], Sheng Sun [2, 3], Peng Ding [1, 4*]

[1] Research Center of Nanoscience and Nanotechnology, College of Sciences, Shanghai University, Shanghai, China

[2] Materials Genome Institute, Shanghai University, Shanghai, China

[3] Zhejiang Laboratory, Hangzhou, China

[4] Shanghai Key Laboratory of Atomic Control and Application of Inorganic 2D Supermaterials，Shanghai University, Shanghai, China

*e-mail: dingpeng@shu.edu.cn

*Corresponding author. E-mail: dingpeng@shu.edu.cn (Peng Ding)

Contents:

PDA modifications (b), High-resolution XPS spectra at C1s for PDA@PI (c), and N1s for CPPG-1400 (d).

Fig. S8. HRTEM image EDS mapping and element distribution of CPPG-1400 (a-d).

Fig. S9. Infrared spectra of three-dimensional skeleton. FTIR spectra of raw material (a), FTIR spectra after graphene impregnation of PI felt with different PDA modifications (b), FTIR spectra of skeleton after high temperature carbonization (c).

Table S3. EMI shielding properties of composites.

Fig. S10. Characterization of electromagnetic shielding properties and thermal properties of composite materials. The composites EMI shielding properties of co-carbonized skeleton with different modification PDA modification ratios (a (SE_A); b (SE_R)) and co-carbonized skeleton with different modification PDA modification ratios (c (SE_A); d (SE_R)); Composite TGA and DTG data (e-f).

Fig. S11. Conductivity data of PI composites.

Table S4. Detailed information on the TC of the composites was obtained with the laser flash technique.

Fig. S12. Finite element simulations of the composites verify their thermal conductivity. Finite element simulation model of PIC (a), CPPC (b), CPPGC (c).

Table S5. The parameters of the materials used in Abaqus simulation.

Fig. S13. Infrared thermographic characterization of the composite warming process.

Fig. S14. Topography and their corresponding 3D images. Topography and their corresponding 3D images of CPPGC-1400 (a-b) and CPPC-1400 (c-d).

Fig. S15. Thermal sensing scanning atomic force microscopy characterization. (a) SThM (c) Topography and (b, f) their corresponding 3D images of PIC.

Table S5. The mass fraction of every component of the composites.

Table S6. Comparison of EMI shielding performance and thermal conductivity of the polymer matrix composites.

Supplementary Methods

Preparation of CPPG carbon heterostructure/PI composites (CPPGC)

The CPPG was dried at 75 °C before use. The 15 wt% PI solution was prepared by dissolving the PI powder in DMF solvent. The felt was immersed in solution under a vacuum to remove air bubbles for 12h. And the solvent was heated at 60 °C for 12h, 100 °C for 12h, 140 °C for 12h, and 165 °C for 1h to evaporate the solution (evaporation and solvent removal time is fine-tuned according to the amount of solvent). Other PI-based composites were prepared by the same process. The mass fraction of each component in the composites was weighed before vacuum infusion:

Table S1. The mass fraction of every component of the composites.

The name of composites	PI (wt%)	CPI (wt%)	CPP (wt%)	CPPG (wt%)
PIC	100	-	-	
CPIC	-	21.22	-	
CPPC	-	-	21.80	
CPPGC-0.25	-	-	-	21.15
CPPGC-0.5	-		-	28.55
CPPGC-1/ CPPGC-1400	-		-	34.04
CPPGC-1.5	-	-	-	41.50

Characterization

The structure and chemical composition of PI fiber and composites were characterized by Fourier-transform infrared spectra (FTIR, AVATAR 370, Nicolet, USA) and X-ray diffraction (XRD, D/max-2200/PC, Rigaku, Japan), X-ray photoelectron spectroscopy (XPS, RBD upgraded PHI 5000C ESCA, PerkinElmer, USA). Thermal diffusivity (α, $mm^2 \cdot s^{-1}$) was measured using a Netzsch LFA 447 Nanoflash instrument at 25 °C. The density (ρ, $g \cdot cm^{-3}$) was determined using a JA3003J electronic balance (SOPTOP, China). The specific heat capacity (Cp, $J \cdot g^{-1} \cdot K^{-1}$) was measured by differential scanning calorimetry (DSC, TA Instruments 250) at room temperature. Thermal conductivity (TC) was calculated using the standard formula: $TC=\rho \times Cp \times \alpha$. In addition, an infrared thermal imaging spectrometer

(Optris PI400, Germany) was used to visually evaluate heat transport behavior. The thermal conductive enhancement (TCE) compared with pure PI composite can be calculated as follow: $TCE(\%) = \frac{TC - TC_{PIC}}{TC_{PIC}}$. Thermogravimetric analysis (TGA) was performed using a TA Q500 HiRes Thermogravimetric analyzer at a heating rate of 10 °C·min^{-1}. The high-temperature in-situ EMI shielding test equipment (PNA N5225B vector network analyzer from Keysight Technologies (USA), equipped with a high-temperature waveguide module). EMI shielding properties of the prepared materials were evaluated from the S parameters, which include four sub-parameters: the forward reflection coefficient (S_{11}), the forward transmission coefficient (S_{21}), the reverse transmission coefficient (S_{12}), and the reverse reflection coefficient (S_{22})[1]. The power coefficient of reflection (R, $R=|S_{11}|^2=|S_{22}|^2$), transmission (T, $T=|S_{21}|^2=|S_{12}|^2$), and absorption (A, A=1-R-T) can be calculated using S-parameters. In addition, the total EMI SE (SE_T), reflection loss (SE_R), and absorption loss (SE_A) can be obtained by the following formula[2, 3]:

$$SE_T = -10\log T$$

$$SE_R = -10\log(1-R)$$

$$SE_A = -10\log\left(\frac{T}{1-R}\right)$$

$$SE_T = SE_R + SE_A$$

In our preceding studies[4-6], carbon fibers, graphene, and their derivatives were incorporated into PI matrices to construct binary carbon heterostructures network, facilitating phonon and electron transport while enhancing interfacial polarization. These strategies resulted in simultaneous improvements in EMI shielding and TC. However, further enhancement remains a challenge due to the limitations of binary structures in achieving optimal EMW dissipation and thermal transport.

To address this, we extended our design framework by leveraging domain knowledge and literature data to guide the construction of a ternary carbon heterostructure network that integrates multiple conductive pathways and hierarchical interfaces. Based on systematically extracted structural and material parameters related to EMI shielding and TC,[7, 8] we employed finite element simulations to predict the electromagnetic and thermal response of the composites. As shown in Fig. 1a-b, models at both microscopic and macroscopic scales were developed to assess the influence of structural configuration on EMI attenuation and heat conduction.

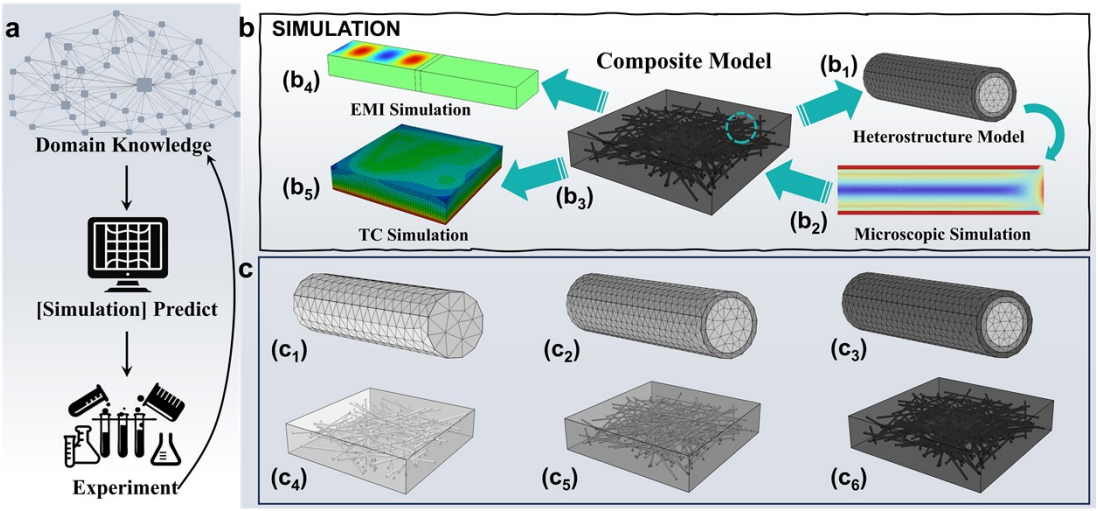

Fig. S1. a, Domain knowledge guided Integrated Computational Materials Engineering (ICME) strategy. **b,** Material modeling guided by Domain knowledge for finite element software simulations: (b_1) a ternary heterostructure carbon fiber mode, (b_2) COMSOL simulation of ternary heterostructure carbon fiber microscopic electromagnetic waves response, (b_3) Modeling of PI composites containing ternary carbon heterostructures, (b_4) Simulation of macroscopic EMI shielding properties of PI composite models, (b_5) Simulation of macroscopic TC properties of PI composite models. **c**, Carbon fiber model for COMSOL Multiphysics field simulation: (c_1) features a single carbon fiber, (c_2) a carbon fiber with a binary heterostructure, (c_3) and a ternary heterostructure carbon fiber, (c_4- c_6) TC and EMI shielding simulation model constructed from the corresponding carbon fiber model.

Fig. S1b$_1$ showcases a microscopic model of a heterostructure carbon fiber, engineered based on expert knowledge. This includes the model of a single carbon fiber, a binary, and a ternary heterostructure of the carbon fiber (Fig. S1c$_{1-3}$), all designed to evaluate their efficacy in dissipating EMWs in complex scenarios (Fig. S1b$_2$). Additionally, macroscopic PI composite models composed of ternary heterostructure carbon fibers were constructed (Fig. S1b$_3$ and Fig. S1c$_{4-6}$), and simulations of their EMI shielding and TC properties were conducted (Fig. S1b$_{4-5}$). This domain knowledge-driven model design provides reliable support for subsequent finite element simulation validations and experimental verifications.

COMSOL Multiphysics software was employed to simulate the electromagnetic response of all-carbon heterostructures under complex electromagnetic environments (detailed parameters in Table S2). Fig. S2a-c illustrates the propagation of the electromagnetic field along the Y-axis in a single carbon fiber at 12 GHz. Compared to homogeneous carbon fibers (Fig. S2a), binary heterostructures exhibit a distinct current density contrast at the interface due to conductivity differences (Fig. S2b). In contrast, ternary heterostructures introduce multiple current density boundaries (Fig. S2c), creating pronounced gradients in material conductivity. These variations generate induction loops, intensifying eddy current losses and enhancing EMW dissipation.[9] Further COMSOL simulations on macroscopic models of PI composites containing ternary heterostructures (Fig. 1b$_4$) demonstrated superior EMW shielding compared to pure PI resins (Fig. S3a-c). The results underscore the critical role of ternary heterostructured interfaces in significantly improving EMI shielding effectiveness (Fig. S3c). To assess thermal transport, we simulated the TC of PI composites containing ternary heterostructure carbon fibers using Abaqus finite element software (Fig. S1c$_{4-6}$, Fig. S1b$_5$). The preliminary results (Fig. S4a-c) reveal that ternary heterostructured composites exhibit the highest TC, with the most pronounced color variation indicating the fastest heat conduction (Fig. S4c).

Integrated Computational Materials Engineering (ICME) accelerates material development by integrating computational simulations with experimental validation[10], significantly reducing time and resource consumption while enabling the precise design of advanced materials and providing deeper insights into electromagnetic and thermal transport mechanisms.[11-13] (Fig. S1a)

Table S2. Parameters related to electromagnetic response and thermal

conductivity simulation model.

Objects	PI matrix resin	carbon fiber	Intermediate carbon layer	Outer carbon layer
Density (g/cm^3)	1.427	1.2	2.2	2.2
Thermal conductivity ($W\ m^{-1}\ K^{-1}$)	0.26	110	600	800
Specific heat capacity ($J\ kg^{-1}\ K^{-1}$)	1075	710	710	710
Electrical conductivity (S/m)		1.9×10^5	2.6×10^5	1×10^8
Magnetic conductivity (H/m)		1	1	1

Abaqus2020 Finite element analysis was used to simulate the transient thermal response during thermal diffusion of the PI matrix composite. the detailed material parameters used for the FEA can be found in Supplementary Table 2. The size of the three simulation models is set to 10 mm×10 mm×2 mm. The initial temperature of the model is set to 0 °C, and a constant heat source of 100 °C is added at the bottom of the model. The convective heat transfer coefficient between the sample and the air is set as a moderate value of 5 $W/m^2\cdot K$, and the ambient temperature is set as 25 ℃. The type of solver we used is Standard, which is computed by Python scripts for Abaqus are developed to computate, the computer model is Intel 10500T CPU and 16384MB RAM. COMSOL's multiphysics simulation environment enables us to model the complex interactions between electromagnetic fields and materials, allowing for a detailed investigation of shielding effectiveness. Supplementary Figs. 3a shows a schematic diagram of the EMI shielding simulation, the sample is placed between ports 1 and 2, port 1 is the EMWs transmitter, and the EMWs is measured at port 2 after it passes through the sample so as to evaluate the EMI shielding performance of the sample. From the macroscopic simulation results, it can be seen that the pure PI material has almost no shielding effect on electromagnetic waves, while the PI composites consisting of ternary carbon heterostructures can almost completely shield electromagnetic waves.

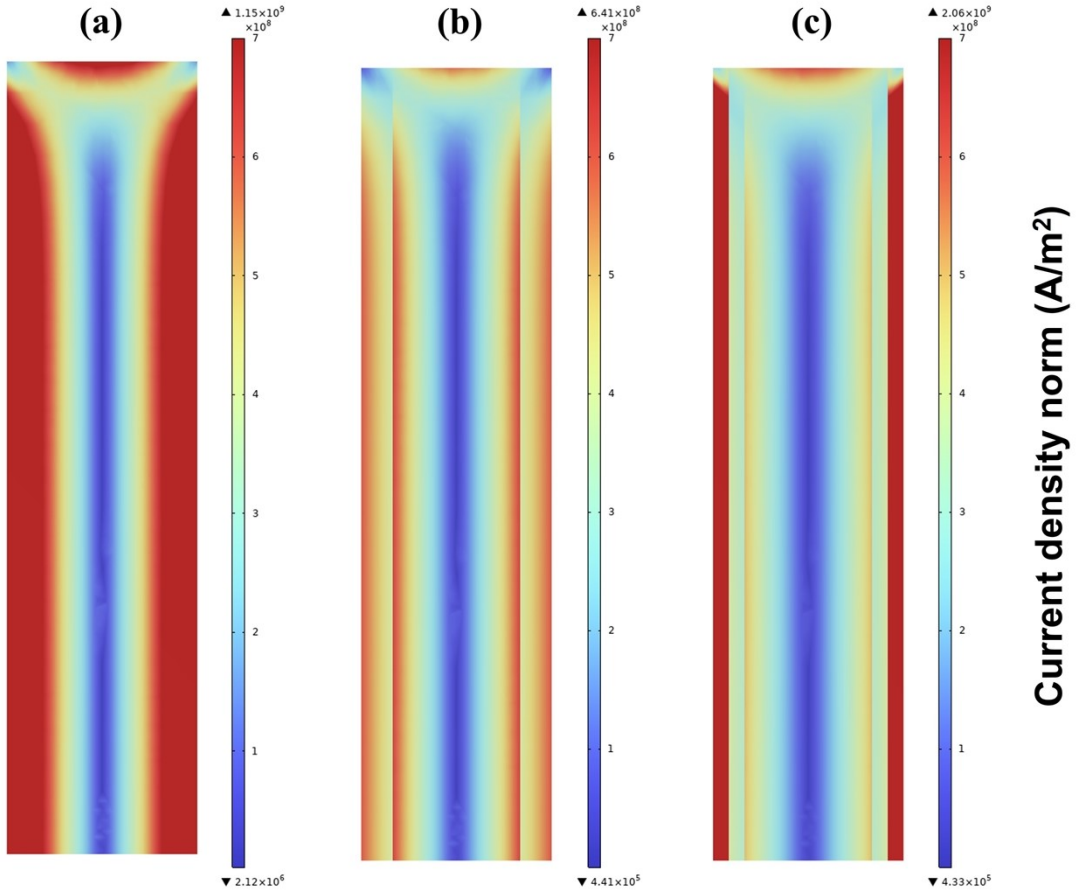

Fig. S2. Characteristic current density diagram of the fiber microstructure in response to an electromagnetic field. (**a**) a single carbon fiber. (**b**) a binary heterostructure carbon fiber. (**c**) a ternary heterostructure carbon fiber model.

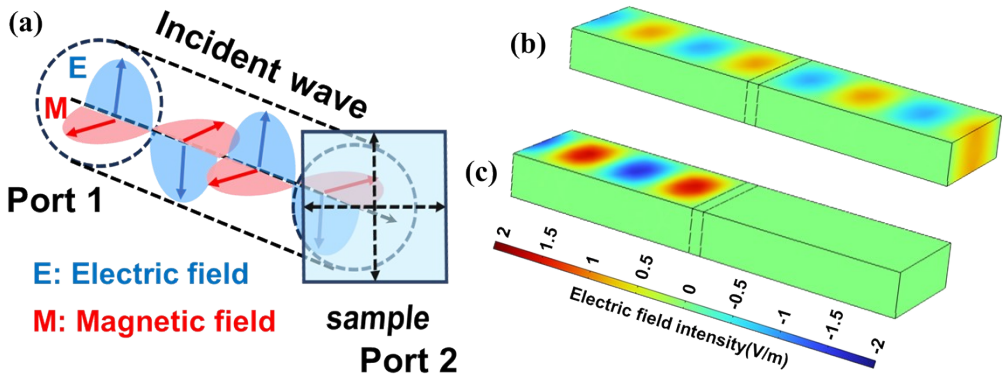

Fig. S3. Simulated macroscopic electromagnetic shielding properties. (**a**) PI composites COMSOL EMI shielding performance test simulations schematic. (**b**) pure PI and (**c**) carbon fiber PI composites containing ternary carbon heterostructure.

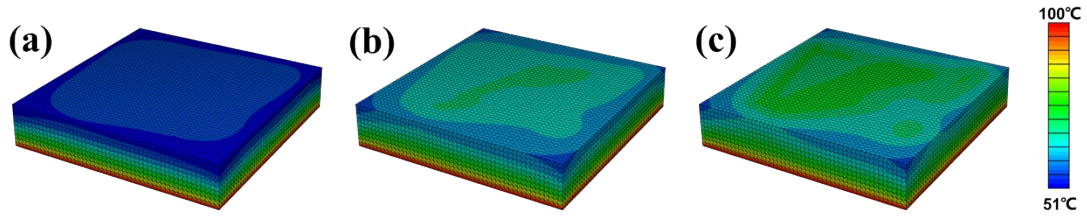

Fig. S4. Schematic representation of the fiber model corresponding to the simulated thermal conductivity properties of PI composites (including meshing): (**a**) a single carbon fiber PI composite. (**b**) a binary heterostructure PI composite. (**c**) a ternary heterostructure carbon fiber PI composite.

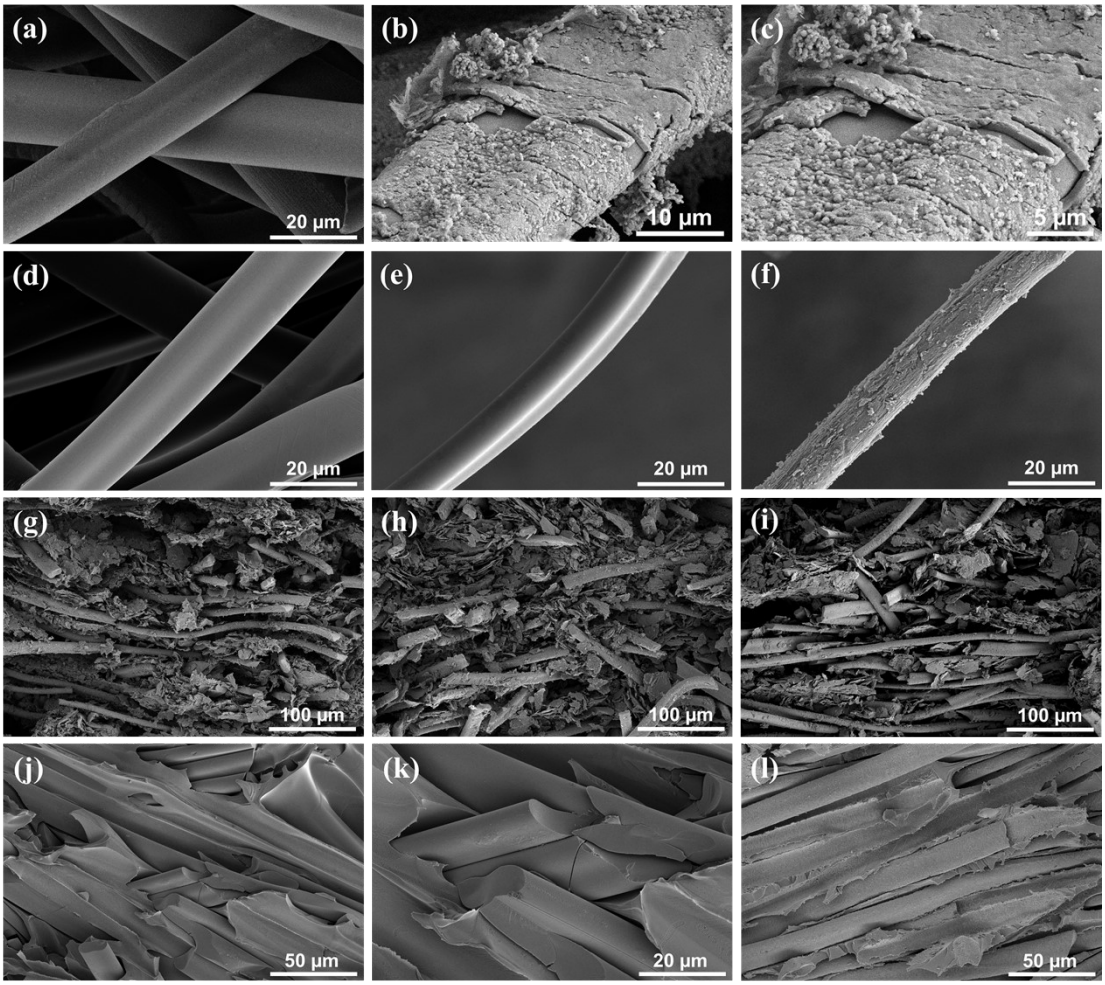

Fig. S5. Fiber Characteristic Structures and SEM Images of Composites. SEM images of raw PI (a), PDA@PI fibers 1:1 (b, c); SEM images of CPI-1200 (d), CPI-1400 (e), CPI-1600 (f); SEM images of CPPG-1000 (g), CPPG-1200 (h), CPPG-1600 (i); SEM images of PI composites CPIC-1400 (d, k), CPPC-1400 (e).

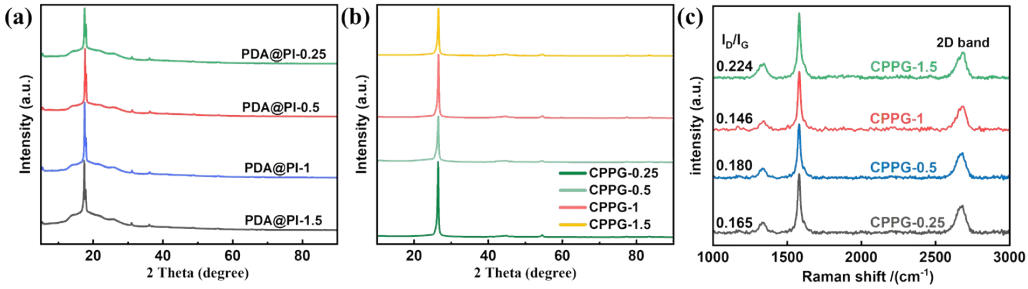

Fig. S6. Modulation of PDA modification ratios to construct heterostructures. XRD spectra of PI felts with different degrees of PDA modification (a), XRD spectra of CPPG skeleton under different PDA modifications (b), Raman spectra of CPPG skeleton under different PDA modifications (c).

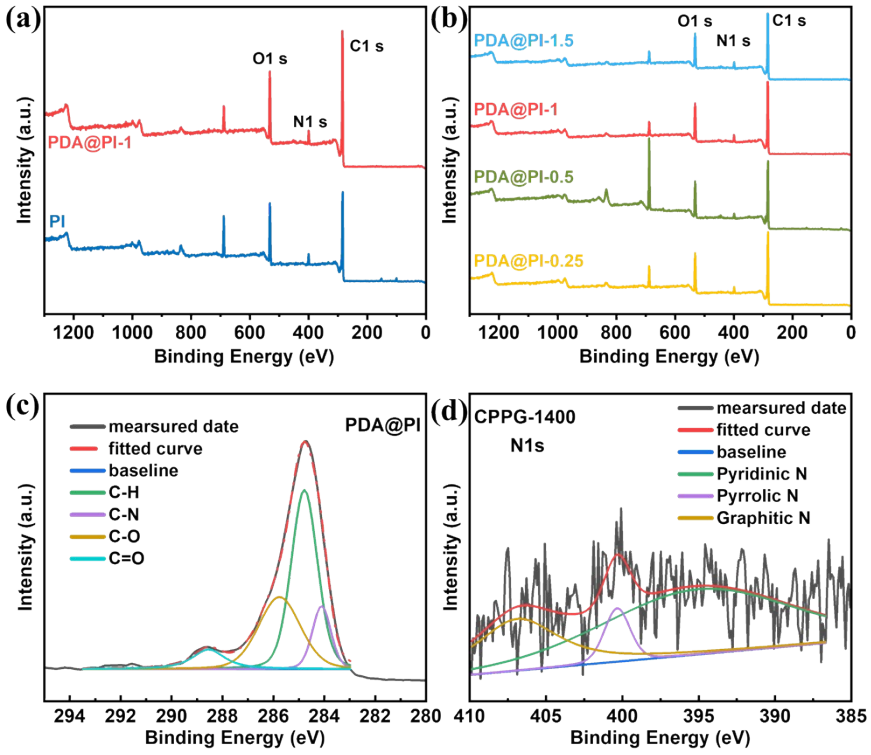

Fig. S7. Three-dimensional skeleton XPS and its peak splitting graphs. XPS spectra of PI felts and PDA@PI (a), XPS spectra of PDA@PI skeleton under different PDA modifications (b), High-resolution XPS spectra at C1s for PDA@PI (c), and N1s for CPPG-1400 (d).

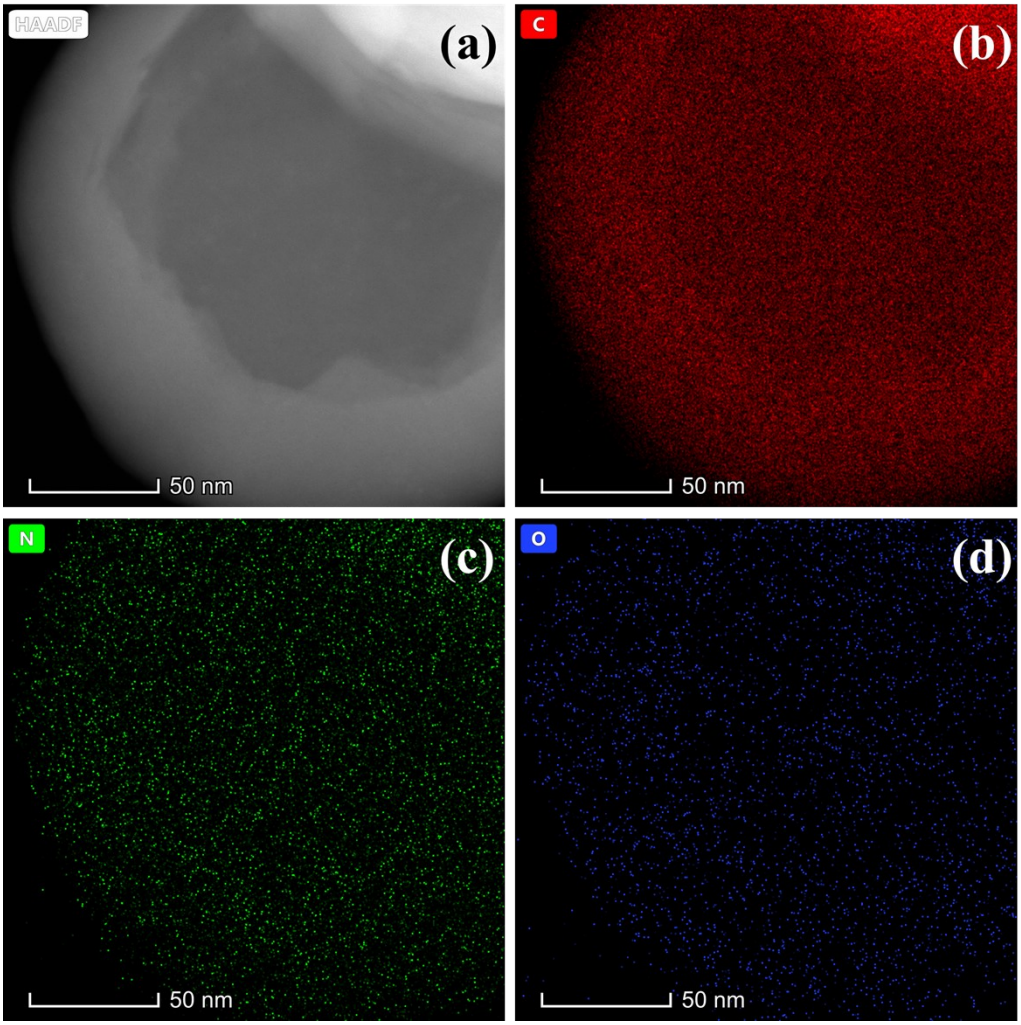

Fig. S8. HRTEM image EDS mapping and element distribution of CPPG-1400 (a-d).

Modification by PDA helps graphene adsorb uniformly and abundantly on the fibers, providing a basis for in situ co-carbonation interface modulation. From the FTIR spectra in Fig. S9a, graphene (G) shows an inert chemical structure with only -OH telescoping vibrational peaks near 3438 cm^{-1}, and the presence of -OH at the edge of G facilitates the formation of hydrogen bonding interactions with fibers. Hydrogen-bonding interactions provide the basis for the strong bonding of graphene to the fibers during the subsequent co-carbonization process. The absorption peak at 3484 cm^{-1} of the PI felt modified with PDA (PDA@PI) is attributed to the stretching vibration of -OH, but it can be seen that the modification with PDA did not chemically react with the molecules on the surface of the PI to generate new products due to the original PI characteristic peaks. For such as the characteristic peaks of the stretching vibration of C=O and the characteristic peak of C=O in the benzene ring at 1716 cm^{-1} and 1776

cm^{-1}, and the characteristic peaks of C-N at 1358 cm^{-1} are unchanged. In contrast, when G was adsorbed onto the PDA@PI backbone, the peak of the stretching vibration of -OH was shifted to 3371 cm^{-1} , indicating the generation of hydrogen bonding interactions[14] ◦ PPG infrared characteristic peak positions did not change much for different PDA modification degrees, as shown in Fig. S9b. The continuous wave peaks formed at 3144 cm^{-1}, 3071 cm^{-1}, 3044 cm^{-1}, and 2957 cm^{-1} in the figure are the asymmetric telescopic vibration peaks of polydopamine enriched with a large amount of -OH[15]. After the high-temperature co-carbonization process we can see that the infrared spectrogram of CPPG is basically devoid of the absorption peaks of functional groups, and most of the organic characteristic peaks disappear completely (Fig. S9c).

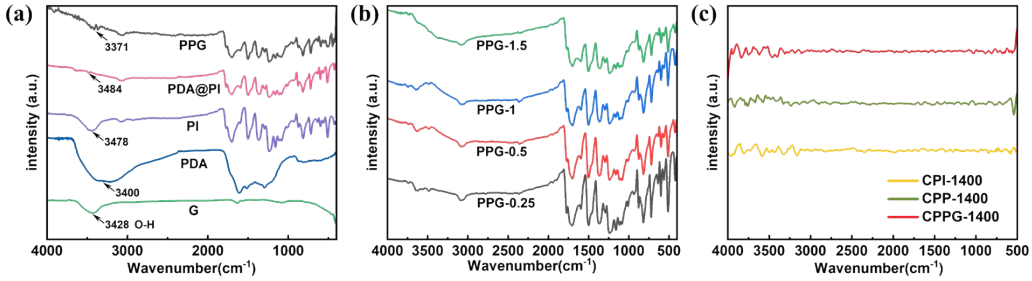

Fig. S9. Infrared spectra of three-dimensional skeleton. FTIR spectra of raw material (a), FTIR spectra after graphene impregnation of PI felt with different PDA modifications (b), FTIR spectra of skeleton after high temperature carbonization (c).

Table S3. EMI shielding properties of composites.

Samples	SE_R (dB)	SE_A (dB)	SE_T (dB)
PIC	0	0	0
CPPGC-1000	9.02	58.86	67.88
CPPGC-1200	0.67	79.00	79.67
CPPGC-1400/CPPGC-1	11.31	83.69	95.00
CPPGC-1600	11.6	46.76	58.36
CPPGC-0.25	18	40.83	58.83
CPPGC-0.5	11.87	56.06	67.93
CPPGC-1.5	12.3	67.24	79.54

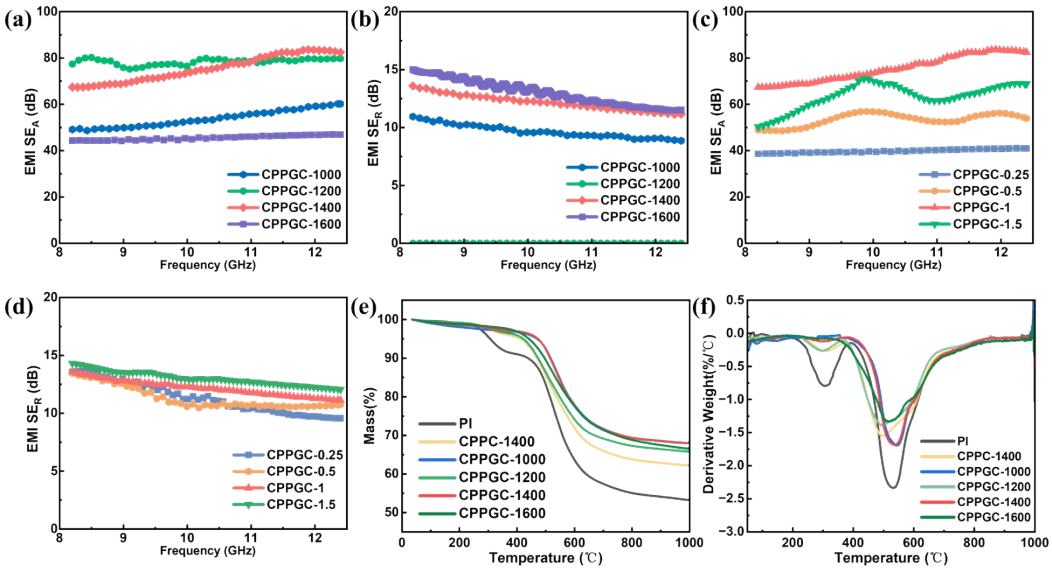

Fig. S10. Characterization of electromagnetic shielding properties and thermal properties of composite materials. The composites EMI shielding properties of co-carbonized skeleton with different modification PDA modification ratios (a (SE_A); b (SE_R)) and co-carbonized skeleton with different modification PDA modification ratios (c (SE_A); d (SE_R)); Composite TGA and DTG data (e-f).

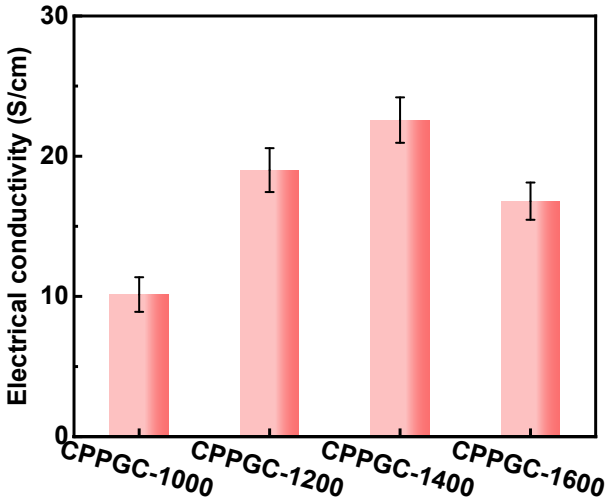

Fig. S11. Conductivity data of PI composites.

Table S4. Detailed information on the TC of the composites was obtained with the laser flash technique.

Samples	α (mm^2/s)	TC ($W \cdot m^{-1}K^{-1}$)	TCE (%)
PIC	0.18	0.27	/
CPIC-1400	0.84	1.01	274.07 %
CPPGC-1000	1.38	2.07	666.66 %
CPPGC-1200	1.62	2.12	685.18 %
CPPGC-1400	2.11	3.38	1151.85 %
CPPGC-1600	2.06	2.87	962.96 %

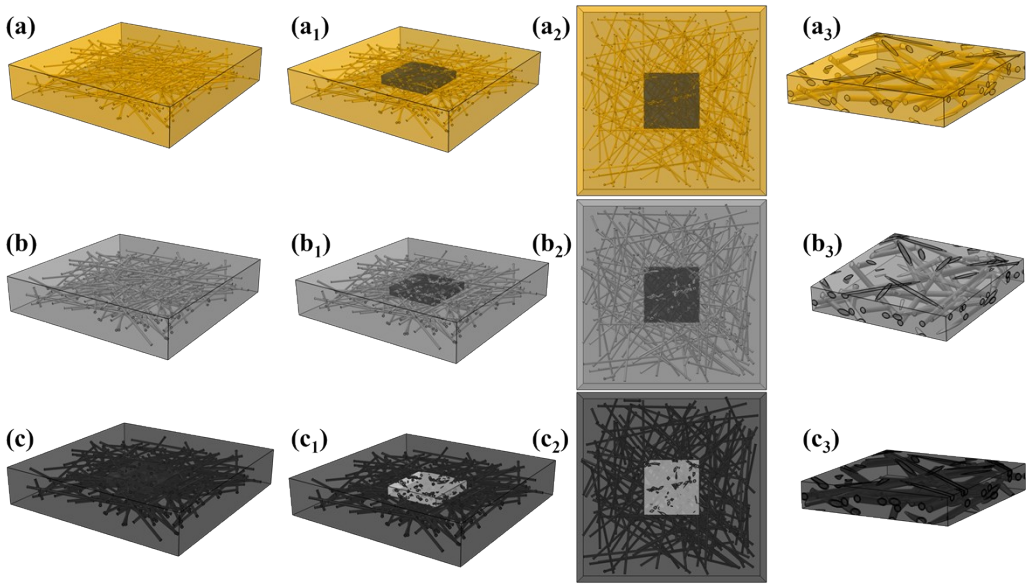

Fig. S12. Finite element simulations of the composites verify their thermal conductivity. Finite element simulation model of PIC (a), CPPC (b), CPPGC (c).

Table S5. The parameters of the materials used in Abaqus simulation.

Objects	Density (g/cm^3)	Thermal conductivity ($W\ m^{-1}\ K^{-1}$)	Specific heat capacity ($J\ kg^{-1}\ K^{-1}$)
PI	1.427	0.26	1075
PI-based carbon fiber	1.181	109.74	712
C-PDA	2.2	600	710
Graphene	2.2	800	710

Figure S13 shows a graph of the thermal management properties of the PI composites on a constant-temperature hotbed with an infrared thermography camera recording the samples, which is a more intuitive response to the thermal conductivity of the prepared composites. The first of these columns is a physical image of the CPPGC composite as well as a pure sample of PI, with the samples simultaneously placed on the surface of a hot table at a constant 80 °C, in the order of the physical image, and on the right side is the warming of the samples recorded by an infrared thermography camera. Through Fig. S13, the color change of CPPGC-1400 composites can be clearly seen to be the most drastic, meaning that the fastest temperature rise is achieved in the same period of time. The infrared thermography results correspond well with the thermal conductivity of the composites, indicating that the CPPGC-1400 composites have the most excellent thermal conductivity and potential thermal management capabilities in practical applications. Moreover, through infrared thermography, the heat transfer of CPPGC-1400 can be visualized not only quickly but also uniformly, which proves that ternary carbon heterojunction network can optimize the TC of the PI composites very well.

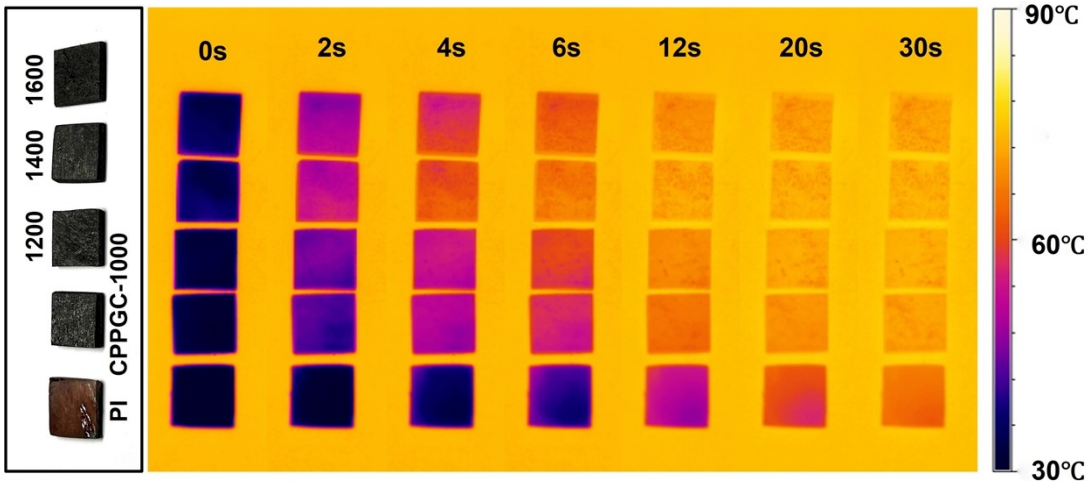

Fig. S13. Infrared thermographic characterization of the composite warming process.

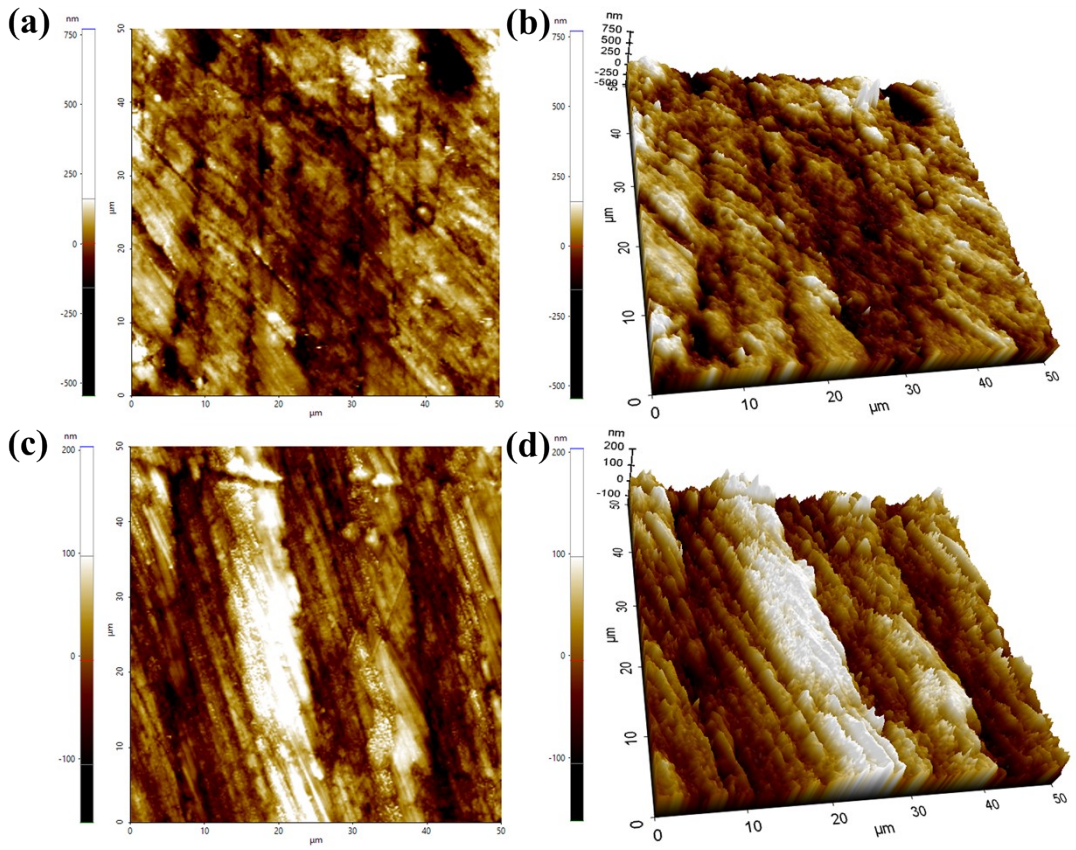

Fig. S14. Topography and their corresponding 3D images. Topography and their corresponding 3D images of CPPGC-1400 (a-b) and CPPC-1400 (c-d).

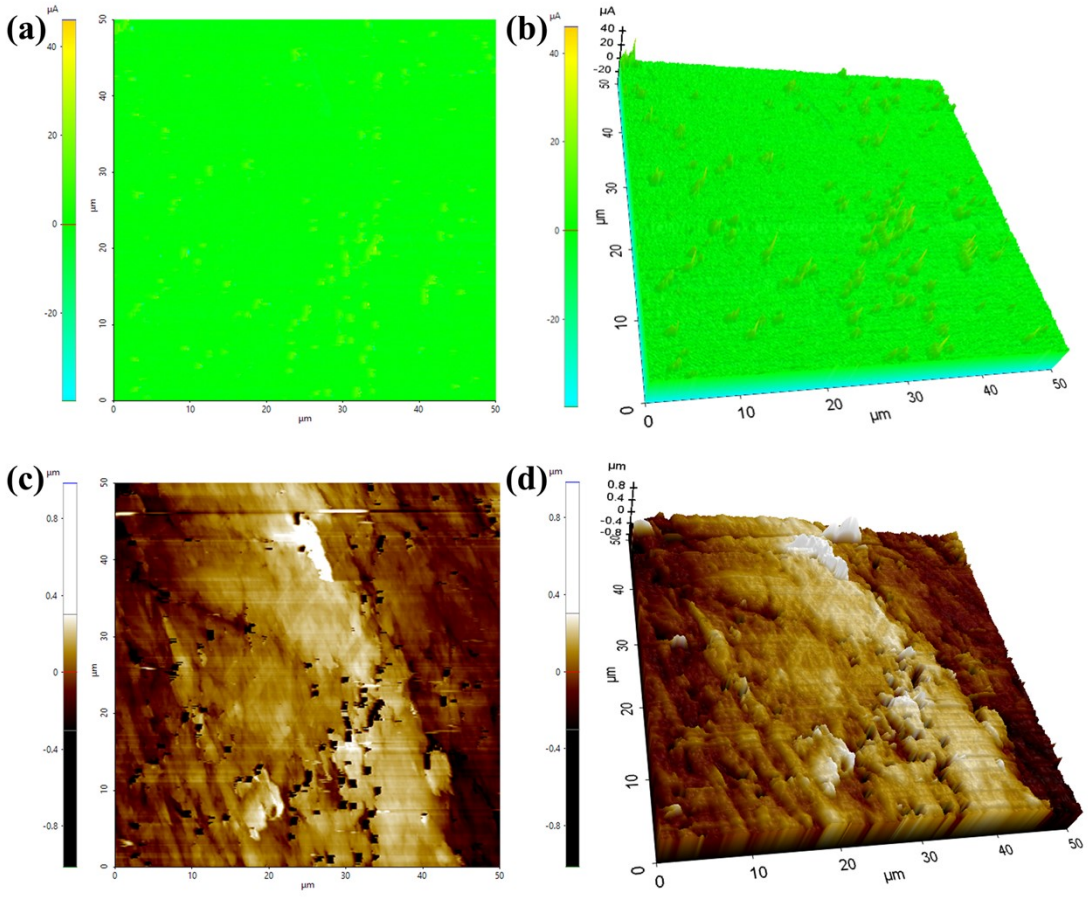

Fig. S15. Thermal sensing scanning atomic force microscopy characterization. (a) SThM (c) Topography and (b, f) their corresponding 3D images of PIC.

Table S5. The mass fraction of every component of the composites.

The name of composites	PI (wt%)	CPI (wt%)	CPP (wt%)	CPPG (wt%)
PIC	100	-	-	
CPIC	-	21.22	-	
CPPC	-	-	21.80	
CPPGC-0.25	-	-	-	21.15
CPPGC-0.5	-		-	28.55
CPPGC-1/ CPPGC-1400	-		-	34.04
CPPGC-1.5	-	-	-	41.50

Table S6. Comparison of EMI shielding performance and thermal conductivity of the polymer matrix composites.

Materials	Thermal conductivity ($W\ m^{-1}\ K^{-1}$)	EMI SE (dB)	Year and references
GNP/PEDOT:PSS	0.6	46	2015[16]
MXene/graphene/PU/ PEG	2.44	43.3	2022[2]
CCA/rGO/PDMS	0.65	51	2021[17]
GNPs/rGO/EP	1.56	51	2019[18]
MXene/PCM	0.74	64.7	2021[19]
CNTs/EP	0.61	35.57	2021[20]
LMPA/ER	1.23	35.56	2022[21]
Mxene/PVDF	0.767	48.47	2020[22]
CuNWs-TAGA/EP	0.51	47	2020[23]
MXrGO@PMMA	3.96	61	2021[24]
CNT/TPU	0.51	42.5	2021[25]
Ag/PPS	1.15	87.8	2021[26]
MDCF@hBN/EP	0.99	52.77	2022[27]
Graphene/carbon fiber/PI	1.65	73	2023[4]

P(St-BA)/GNS@PDA	1.68	58	2021[28]
MF-10/EP	0.46	35	2019[29]
MXene/G/PEG	1.64	36	2022[30]
CPPGC-1400/CPPGC-1	**3.38**	**95**	**This work**

References

1. F. Shahzad, M. Alhabeb, C. B. Hatter, B. Anasori, S. Man Hong, C. M. Koo and Y. Gogotsi, *Science*, 2016, **353**, 1137-1140.
2. L. Jin, W. Cao, P. Wang, N. Song and P. Ding, *Nano-Micro Lett.*, 2022, **14**, 133.
3. S. Gupta and N. H. Tai, *Carbon*, 2019, **152**, 159-187.
4. X. Li, T. Xu, W. Cao, M. Wang, F. Chen, L. Jin, N. Song, S. Sun and P. Ding, *Chem. Eng. J.*, 2023, **464**, 142595.
5. T. L. Xu, S. S. Zhou, F. Jiang, N. Song, L. Y. Shi and P. Ding, *Compos. Part B: Eng.*, 2021, **224**.
6. T. L. Xu, S. S. Zhou, S. Q. Cui, N. Song, L. Y. Shi and P. Ding, *Compos. Part B: Eng.*, 2019, **178**.
7. X. Huan, H. Wang, W. Deng, J. Yan, K. Xu, H. Geng, X. Guo, X. Jia, J. Zhou and X. Yang, *Small*, 2022, **18**, e2105411.
8. G. Wang, C. Li, D. Estevez, P. Xu, M. Peng, H. Wei and F. Qin, *Nano-Micro Lett.*, 2023, **15**, 152.
9. Y. Bai, L. Zhao, D. Ju, Y. Jiang and L. Liu, *Opt. Express*, 2015, **23**, 8670-8680.
10. Z. Huang, R. Shi, X. Xiao, H. Fu, Q. Chen and J. Xie, *Mater. Today Commun.*, 2021, **27**, 102378.
11. W. Cao, X. Li, Y. Chen, L. Jin, R. Guo, N. Song, S. Sun and P. Ding, *Adv. Funct. Mater.*, 2024, **35**.
12. S. Zhou, T. Xu, N. Song, J. Dai, G. Qian and P. Ding, *Chem. Eng. J.*, 2024, **481**.
13. D. Xu, Y. Yang, L. Lyu, A. Ouyang, W. Liu, Z. Wang, L. Wu, F. Yang, J. Liu and F. Wang, *Chem. Eng. J.*, 2021, **410**.
14. N. Song, P. Wang, L. Jin, F. Zhang, Z. Wang and P. Ding, *Chem. Eng. J.*, 2022, **437**, 135404.
15. L. Li, B. Zhou, G. Han, Y. Feng, C. He, F. Su, J. Ma and C. Liu, *Compos. Sci. Technol.*, 2020, **197**, 108229.
16. N. Agnihotri, K. Chakrabarti and A. De, *Rsc. Adv.*, 2015, **5**, 43765-43771.
17. P. Song, B. Liu, C. Liang, K. Ruan, H. Qiu, Z. Ma, Y. Guo and J. Gu, *Nano-Micro Lett.*, 2021, **13**, 91.
18. C. B. Liang, H. Qiu, Y. Y. Han, H. B. Gu, P. Song, L. Wang, J. Kong, D. P. Cao and J. W. Gu, *J. Mater. Chem. C*, 2019, **7**, 2725-2733.
19. H. B. Liu, R. L. Fu, X. Q. Su, B. Y. Wu, H. Wang, Y. Xu and X. H. Liu, *Compos. Sci. Technol.*, 2021, **210**, 108835.
20. Z. Zong, F. Ren, Z. Z. Guo, Z. X. Lu, Y. L. Jin, Y. C. Zhao and P. G. Ren, *Composites Part B: Engineering*, 2021, **223**, 109132.
21. P. Zhang, R. Tian, X. Zhang, X. Ding, Y. Wang, C. Xiao, K. Zheng, X. Liu, L. Chen and X. Tian, *Composites Part B: Engineering*, 2022, **232**, 109611.
22. K. Rajavel, S. B. Luo, Y. J. Wan, X. C. Yu, Y. G. Hu, P. L. Zhu, R. Sun and C. P. Wong, *Compos. Part A-Appl. S.*, 2020, **129**, 105693.
23. X. Yang, S. Fan, Y. Li, Y. Guo, Y. Li, K. Ruan, S. Zhang, J. Zhang, J. Kong and J. Gu, *Compos. Part A-Appl. S.*, 2020, **128**, 105670.
24. M. C. Vu, D. Mani, J.-B. Kim, T.-H. Jeong, S. Park, G. Murali, I. In, J.-C. Won, D. Losic, C.-S. Lim and S.-R. Kim, *Compos. Part A-Appl. S.*, 2021, **149**, 106574.
25. B. Shin, S. Mondal, M. Lee, S. Kim, Y. I. Huh and C. Nah, *Chem. Eng. J.*, 2021, **418**, 129282.
26. W. Ren, Y. Yang, J. Yang, H. Duan, G. Zhao and Y. Liu, *Chem. Eng. J.*, 2021, **415**, 129052.
27. Y. X. Qian, Y. Tao, Y. Li, J. N. Hao, C. C. Xu, W. Yan, Q. H. Jiang, Y. B. Luo and J. Y. Yang, *Chem. Eng. J.*, 2022, **441**, 136033.
28. L. F. Wei, J. Z. Ma, W. B. Zhang, S. L. Bai, Y. N. Ren, L. Zhang, Y. K. Wu and J. B. Qin, *Carbon*, 2021, **181**, 212-224.
29. L. Wang, H. Qiu, C. B. Liang, P. Song, Y. X. Han, Y. X. Han, J. W. Gu, J. Kong, D.

Pan and Z. H. Guo, *Carbon*, 2019, **141**, 506-514.
30. L. Jin, P. Wang, W. Cao, N. Song and P. Ding, *ACS Appl. Mater. Interfaces*, 2022, **14**, 1747-1756.